INTERNATIONAL JOURNAL FOR NUMERICAL METHODS IN FLUIDS
Int. J. Numer. Meth. Fluids 2003; **41**:339–355 (DOI: 10.1002/fld.439)

A numerical method for inverse design based on the inverse Euler equations

A. Scascighini, A. Troxler*,† and R. Jeltsch

Seminar for Applied Mathematics, ETH Zurich, CH-8092, Zurich, Switzerland

SUMMARY

We present a numerical method for the inverse shape design of internal flows based on the inverse Euler equations (Keller JJ, *Physics of Fluids* 1999; **11** and *Zeitschrift für Angewandte Mathematik und Physik* 1998; **49**). We describe an efficient numerical method based on a finite difference discretization and on a Newton–Krylov solver. After showing that the three-dimensional (3D) inverse Euler equations hold only for complex lamellar flows, we extend the basic axis-symmetric flow model to handle viscous effects by means of a distributed loss model and to handle quasi-3D effects by deriving a quasi-3D formulation of the inverse Euler equations from the passage averaged 3D Euler equations. The coupling of the 2D inverse Euler equations with an integral boundary layer method is presented too. Copyright © 2003 John Wiley & Sons, Ltd.

KEY WORDS: inverse Euler equations; inverse design; target-pressure-problem; internal flows; quasi-three-dimensional (Q3D); distributed loss model

1. INTRODUCTION

One of the main goals of aerodynamic design of gas turbine components is the reduction of losses due to e.g. viscous effects, shocks in the blade rows or separation. Most of these losses can be controlled or at least limited by a judicious choice of the pressure gradient acting on the walls of the device. For example, separation can be avoided by reducing the adverse pressure gradient. Therefore, solving the *target-pressure-problem* (for diffusers) which reads

> find the shape of a diffuser which generates a given, target pressure distribution along its side walls

is a possible way to increase the performance of a turbine.

*Correspondence to: A. Troxler, Seminar for Applied Mathematics, ETH Zurich, CH-8092 Zurich, Switzerland.
†E-mail: atroxler@sam.math.ethz.ch

Contract/grant sponsor: Alstom Power (Switzerland) Ltd.; contract/grant number: 4571.1 KTS
Contract/grant sponsor: Commission for Technology and Innovation (KTI); contract/grant number: 4571.1 KTS

Received September 2001
Revised 10 August 2002

Three main approaches have been applied to the target-pressure-problem, the optimization approach, the inverse design approach and the trial and error method. The simplest of the three methods, the trial and error approach, is widely used in gas turbine industry: the iterative process consisting in defining a geometry, solving the flow equations and comparing the resulting pressure distribution along the side walls to the prescribed one, is repeated until a satisfactory matching is found. The advantage of this approach lies in its simplicity, disadvantages are the time-consuming procedure and the limited improvement of the devices.

An optimized diffuser shape can be found in an automatic way by solving an optimization problem, such as minimization of viscous losses or of deviation from a given target pressure (e.g. Reference [1]). The strength of the optimization approach lies in its generality and in the fact that it can be fully automated, the disadvantages are the high computing time and resources needed.

The third class of methods, the inverse design approaches, directly solve the target-pressure problem by specifying the target pressure as a boundary condition. The advantage of these methods lies in their speed, since the most CPU intensive step in an optimization method, the computation of gradients, is avoided. The inverse methods are based either on a moving grid strategy [2, 3] or on an intrinsic streamline aligned system of co-ordinates [4–8]. Methods implementing the second strategy are called single-pass methods. Approaches based on a moving grid strategy can be applied to complex, three-dimensional (3D) viscous flows [2], but the convergence to the final geometry is usually very slow (an exception is the method developed in Reference [3]). On the other side, single pass methods converge quickly but the domain of application is more restricted. They have been applied to 2D potential [8] and rotational flows [7], axis-symmetric flows without swirl [6] and 3D potential flows [8, 9]. One of the results of this paper is to delimit the domain of application of the single pass methods (Section 2.5). In the applications we have in mind (design of exhaust diffusers and burning chambers) the geometries are axis-symmetric and the flows can be described by a quasi 3D approximation. Therefore, we develop an extension of the existing single pass axis-symmetric design methods to handle quasi 3D effects.

In this work, we follow the Ansatz of References [4, 5] in which one reformulates the Euler equations in a streamline-based system of co-ordinates and then applies the hodograph transformation. We precise the original formulation of Keller's inverse Euler equations by specifying a set of boundary conditions as well as the details of a numerical method for their efficient solution. As already mentioned above, one of our main contributions is an analysis of the validity of the 3D inverse Euler equations (and related methods), which are shown to hold only for a limited class of flows, and not for general 3D flows in channels. Starting from this negative result we develop a series of enhancements of the basic axis-symmetric inverse Euler equations to incorporate losses caused by shocks via a distributed loss model [10] as well as losses in a boundary layer by an integral method. Three dimensional effects such as blockage and deflection due to the presence of blades can be described in an economical, but nevertheless accurate way by a quasi-3D (Q3D) flow model. We take these phenomena into account in a novel inverse formulation of the Q3D flow equations described in Reference [11].

This paper is structured as follows. In Section 2, we review the work of Keller [4, 5] and show that the 3D inverse Euler equations hold only for a limited class of flows. Section 3 is devoted to the description of the numerical method, which is then applied to a practical example in Section 4. In Section 5, we extend the basic equations to a novel Q3D inverse

formulation and in Section 6 we describe a boundary-layer method which is coupled to the 2D inverse Euler equations.

2. KELLER'S INVERSE EULER EQUATIONS

In this section, we review the work of Keller [4, 5]. The goal is to present the main ingredients of his derivation of the inverse Euler equations. These basic ideas will be useful for understanding the limitations of the 3D inverse Euler equations, as well as for understanding the modifications needed to handle viscous and quasi-3D effects. Details can be found in Reference [12].

2.1. Flow equations

We consider an axis-symmetric, isentropic, but not homentropic, flow which satisfies the non-conservative Euler equations in Crocco's form

$$\partial_x(\rho r u) + \partial_r(\rho r v) = 0 \tag{1a}$$

$$\nabla H - T\nabla s - \frac{C}{r^2}\nabla C = \mathbf{u}^{\perp}\omega \tag{1b}$$

$$\mathbf{u}\cdot\nabla C = 0 \tag{1c}$$

$$\mathbf{u}\cdot\nabla H = 0 \tag{1d}$$

$$\mathbf{u}\cdot\nabla s = 0 \tag{1e}$$

where $\mathbf{u} = (u, v)^{\mathrm{T}}$, $\mathbf{u}^{\perp} = (v, -u)^{\mathrm{T}}$, u, v, w are the velocity components in axial, radial and azimuthal direction, ρ is the density, p the static pressure, $H = c_p T + \frac{1}{2}(u^2 + v^2 + w^2)$ the total enthalpy, s the entropy, $C = rw$ the angular momentum. $\omega = \partial_x v - \partial_r u$ denotes the vorticity. We assume that the flow is smooth and therefore the entropy is constant along a streamline, but not necessarily across the flow; each streamline can have a different level of entropy, thus generating vorticity and rotational effects. C, H, s are called integrals of motion since constant along a streamline by (1c), (1d) and (1d). We recall that for smooth flows and away from stagnation points (1) is equivalent to the Euler equations in conservation form. The aim of the next section is to reformulate (1) in such a way the shape design problem can be easily solved.

2.2. Inverse Euler equations

In the target pressure problem the geometry of the flow device in which (1) holds is not known *a priori*. By a judicious choice of the independent co-ordinates, we can nevertheless define a fixed, *a priori* known computational domain.

We introduce the natural co-ordinate σ by

$$h\nabla\sigma = \frac{\mathbf{u}}{\|\mathbf{u}\|} \tag{2}$$

where h is an integrating factor which ensures the existence of the 'potential' σ even for rotational flows. Further we introduce a stream-function ψ by

$$\nabla\psi = r\rho\mathbf{u}^{\perp} \tag{3}$$

in such a way that the mass conservation (1a) is automatically satisfied. We call (σ, ψ) the inverse co-ordinates. The key observation of many inverse methods [6, 7] is that the stream-function ψ is constant along the unknown walls of the diffuser, independently of their shape. In other words, the flow device is always mapped onto a known and fixed rectangle in inverse co-ordinates. Keller's idea was to rewrite (1) in inverse co-ordinates and to introduce the geometry variables x, r, h instead of the flow variables $\rho, \mathbf{u}, H$. Carrying out some tedious algebra [5] an inverse formulation of the Euler equations is found:

$$\partial_\psi H - T\,\partial_\psi s - \frac{C}{r^2}\,\partial_\psi C = \frac{1}{\rho r J}\,\partial_\psi\left(\frac{h^2}{\rho r J}\right) \tag{4a}$$

$$\partial_\sigma C = 0 \tag{4b}$$

$$\partial_\sigma H = 0 \tag{4c}$$

$$\partial_\sigma s = 0 \tag{4d}$$

where J is the Jacobi determinant of the co-ordinate transformation. The inverse formulation of the Euler equations (4) reduces to four ordinary differential equations instead of five partial differential equations (1).

The mapping $\mathbf{x} = \mathbf{x}(\sigma, \psi) = (x(\sigma, \psi), r(\sigma, \psi))^{\mathrm{T}}$ is not yet defined. By comparing the definitions (2) and (3) we find

$$\mathbf{x}_\sigma = \frac{h^2}{J}\,\mathbf{x}_\psi^{\perp} \tag{5}$$

The first-order system (5) is not quasi-linear. Its linearization is elliptic and unfortunately it is not well suited for the development of a reliable and fast numerical method. Therefore, distancing ourselves a little bit from the original formulation of Keller, we substitute (5) by the corresponding second-order system

$$\partial_\sigma\left(\frac{J}{h^2}\,\partial_\sigma\mathbf{x}\right) + \partial_\psi\left(\frac{h^2}{J}\,\partial_\psi\mathbf{x}\right) = 0 \tag{6}$$

which is found by cross differentiation. In this step we lose *a priori* the orthogonality of the grid. Numerical computations and Proposition 1 below, show that the orthogonality of the grid is maintained. We call the non-linear system of partial differential equations (4) and (6) inverse Euler equations.

The isolines of σ and ψ generate an orthogonal grid since $\nabla\sigma \cdot \nabla\psi = 0$. This property of the grid is not directly present in system (6), but we can show the

Proposition 1
For each sufficiently smooth solution of the non-linear elliptic problem

$$\mathbf{x}_{\sigma,\sigma} + \mathbf{x}_{\psi,\psi} = 0 \quad \text{in } \Omega \tag{7}$$

$$\mathbf{x}_\sigma \cdot \mathbf{x}_\psi = 0 \quad \text{on } \partial\Omega \tag{8}$$

it holds that

$$\mathbf{x}_\sigma \cdot \mathbf{x}_\psi = 0 \quad \text{in } \Omega \tag{9}$$

In particular the grid generated from an isentropic, incompressible flow, i.e. for $h^2/J = 1$, is orthogonal.
The proof consists in showing that $g(\sigma, \psi) = \mathbf{x}_\sigma \cdot \mathbf{x}_\psi$ satisfies a Laplace equation with homogeneous Dirichlet boundary conditions and therefore, by invoking the maximum principle, must vanish identically.

The inverse Euler equations can be interpreted as a special type of grid generation procedure. In fact the scaled Laplace equations (6) are well known in the field of elliptic grid generation [13]. Elliptic grid generation procedures are characterized by the procedure they use to place the grid lines, i.e. where to refine. In the inverse Euler equations, the position of the grid lines, or of the streamlines, is determined by the factor $\Phi = h^2/J$. This geometrical factor is found by solving the momentum conservation (4a). We can therefore say that our method for inverse design consists in a grid generation procedure driven by physical considerations for placing the grid lines.

2.3. *Geometry—flow field relations*

Geometry and flow variables are coupled by definitions (2) and (3). For the specific massflow $m := \|\rho \mathbf{u}\|$ we find the following relation:

$$m = \frac{1}{r} \|\nabla \psi\| = \frac{1}{rJ} \|\mathbf{x}_\sigma\| = \frac{1}{r\|\mathbf{x}_\psi\|} = \frac{h}{rJ} \tag{10}$$

In an isentropic flow we can relate the specific massflow to the remaining variables by the isentropic relations [4]. The stagnation quantities ρ_0, p_0, T_0 are known from the inlet boundary conditions and do not need to be constant everywhere. The rotational effects are given by non-vanishing ψ-derivatives of the stagnation quantities, while the entropy production in a viscous flow can be modelled by a non-vanishing σ-derivative of the same quantities, see Section 5.2.

Since the flow—geometry relations (10) give a direct connection between specific massflow and geometrical factors, we exclusively work with the specific massflow, even if the concept of the target pressure, being more intuitive, is kept in mind. The target pressure problem is transformed into the equivalent target specific massflow problem.

2.4. *Computational domain and boundary conditions*

We prescribe boundary conditions which coincide with standard boundary conditions for subsonic internal flows:

At inlet: we impose the stagnation temperature T_0, the stagnation pressure p_0, the angular momentum C and the flow angle in the meridional plane. In this way we can compute the values of all the integrals of motion.
At outlet: we prescribe a static pressure distribution. As described in Section 2.3 we first convert it to a specific massflow distribution m_{outlet}. The boundary condition looks then like

$$\frac{h^2}{J} - m_{\text{outlet}}^2 J r^2 = 0 \tag{11}$$

On a side wall (*direct*): we impose the geometry of the wall by means of an algebraic equation

$$f(x,r)=0 \tag{12}$$

On a side wall (*inverse*): we impose a pressure distribution $p(\sigma)$. By means of relation (10) this boundary condition is implemented as

$$r^2\|\mathbf{x}_\psi\|^2=\frac{1}{m_{\text{wall}}^2} \tag{13}$$

where m_{wall}^2 is the specific massflow corresponding to $p(\sigma)$.

These boundary conditions fully determine the flow in the domain. For solving the inverse Euler equations we need the following additional boundary conditions which define the grid:

Orthogonality BC: the grid must be orthogonal, therefore following Proposition 1 we impose on the whole boundary the condition

$$\mathbf{x}_\sigma\cdot\mathbf{x}_\psi=0 \tag{14}$$

Length BC: the ordinary differential equation (4a) needs an initial value. We impose the distribution of the integrating factor h along the $\psi=0$ boundary by

$$h=1 \tag{15}$$

We recall that this is equivalent to fixing the length of one streamline.
Translation BC: the shape of the diffuser can be translated and rotated and still satisfy the inverse Euler equations. In order to exclude the possibility of a translation we need to fix one point. For example we impose

$$\mathbf{x}(0,0)=\mathbf{0} \tag{16}$$

We take care of the rotational invariance of the solution by means of the inlet boundary condition which sets the flow angle, and hence the orientation of the inlet surface.

Our choice of independent co-ordinates allows us to define a rectangular computational domain $[0,\sigma_{\max}]\times[0,\psi_{\max}]$. The value of $\sigma_{\max}$ is set to be equal to the length of the reference streamline at $\psi=0$. The value of $\psi_{\max}$ is by definition equal to the total massflow through the channel

$$\psi_{\max}=\int_{\text{inlet}}\rho\mathbf{u}\cdot\mathbf{n}\,\mathrm{d}o \tag{17}$$

In the case of an inverse computation the height of the channel is not defined *a priori*. The designer must prescribe the value of $\psi_{\max}$, and the height of the channel will adjust itself to generate the correct massflow. The situation is different in the case of a direct computation where both side walls are fixed. The value of $\psi_{\max}$ must be iteratively updated by integrating (17).

2.5. Remarks on 3D and viscous flows

One of the main contributions in Reference [4] was the extension of the ideas presented above to three dimensions. We will show in this section that unfortunately the 3D inverse Euler equations hold only for a restricted class of flows.

The definition of the natural co-ordinate σ for a 3D velocity field is

$$h\nabla\sigma = \frac{\mathbf{u}}{\|\mathbf{u}\|} \tag{18}$$

where now $\mathbf{u} \in \mathbb{R}^3$ is the velocity vector in Cartesian co-ordinates. The simple computation

$$\mathbf{u} \cdot \nabla \times \mathbf{u} = (\|\mathbf{u}\|h)\nabla\sigma \cdot (\nabla(h\|\mathbf{u}\|) \times \nabla\sigma + (h\|\mathbf{u}\|)\nabla \times \nabla\sigma) = 0 \tag{19}$$

proves

Proposition 2
The integrating factor h and the natural co-ordinate σ exist if and only if

$$\mathbf{u} \cdot \nabla \times \mathbf{u} = 0 \tag{20}$$

In particular h and σ exist for 2D and axis symmetric rotational flows, or for 3D potential flows.

Flows satisfying (20) are called complex lamellar [14]. From Proposition 2 it follows that we cannot expect the existence of the natural co-ordinate for a general flow, and therefore Keller's construction of the inverse Euler equation cannot be applied. An example of a flow not satisfying (20) is a free vortex generated by the velocity vector $\mathbf{u} = (-y, x, 1)^{\mathrm{T}}$. Since this kind of flows is very common in turning ducts, the 3D inverse equations lose their validity, resp. they will have no solution or produce a non-physical flow.

Another difficulty arises with viscous flows. Along solid side walls the velocity vanishes due to the no-slip condition $\mathbf{u} = 0$. In consequence, it is no longer possible to define a stream function according to (3): the co-ordinate transformation $(x, r) \to (\sigma, \psi)$ becomes singular along solid side walls. Even if this singularity might be removable by scaling the stream function appropriately, it is intuitively clear that in case of separated flows streamlines can not be used as co-ordinates.

The above objections can be softened in two ways. First, 3D effects can be modelled by a Q3D flow model (Section 5), if the geometry under consideration allows for this possibility. Second, if viscous effects are limited to small regions close to the side walls, they can be accounted for by a boundary-layer method (Section 6). Both extensions are very useful for design purposes, as they allow for a remarkable saving in computing time when compared to fully 3D or viscous computations.

3. DISCRETIZATION AND SOLUTION PROCEDURE

We describe a numerical method for the solution of the inverse Euler equations. Since the flow is smooth, a discretization based on finite differences and a Newton–Krylov solver are chosen.

3.1. Discretization

On the computational domain $[0, \sigma_{\max}] \times [0, \psi_{\max}]$ we introduce a uniform grid with spacing $\Delta\sigma = \sigma_{\max}/N_\sigma$ and $\Delta\sigma = \psi_{\max}/N_\psi$, where N_σ, N_ψ are the number of cells in σ resp. ψ direction. The grid points are $(\sigma_i, \psi_j) = (\Delta\sigma\, i, \Delta\psi\, j)$ for $i = 0, \ldots, N_\sigma,\ j = 0, \ldots, N_\psi$. The unknowns in the inverse Euler equations are x, r, h. For sake of an easier implementation, we prefer to work with $\Phi := h^2/J$ instead of h. The nodal values of the unknowns are denoted by $x_{i,j} = x(\sigma_i, \psi_j), \ldots$.

On this grid we introduce the standard difference operators

$$D_\sigma^0 f(\sigma_i, \psi_j) = \frac{f(\sigma_i + \Delta\sigma, \psi_j) - f(\sigma_i - \Delta\sigma, \psi_j)}{2\Delta\sigma} \tag{21}$$

$$D_\sigma^+ f(\sigma_i, \psi_j) = \frac{f(\sigma_i + \Delta\sigma, \psi_j) - f(\sigma_i, \psi_j)}{\Delta\sigma} \tag{22}$$

$$D_\sigma^- f(\sigma_i, \psi_j) = \frac{f(\sigma_i, \psi_j) - f(\sigma_i - \Delta\sigma, \psi_j)}{\Delta\sigma} \tag{23}$$

and their counterparts in ψ direction.

The scaled Laplace equations (6) are discretized as

$$\frac{1}{\Phi_{i,j}} D_\sigma^+ D_\sigma^- \mathbf{x}_{i,j} + \Phi_{i,j} D_\psi^+ D_\psi^- \mathbf{x}_{i,j} + D_\sigma^0 \left(\frac{1}{\Phi_{i,j}} \right) D_\sigma^0 \mathbf{x}_{i,j} + D_\psi^0 \Phi_{i,j} D_\psi^0 \mathbf{x}_{i,j} = 0 \tag{24}$$

for $i = 1, \ldots, N_\sigma - 1, j = 1, \ldots, N_\psi - 1$.

The ordinary differential equation (4a) is discretized by the trapezoidal rule.

The boundary conditions are discretized by second-order one-sided finite differences. As an example on $\psi = \psi_{\max}$ we apply

$$\partial_\psi \mathbf{x}_{i,j} \approx \left(\frac{3}{2}\, \mathbf{x}_{i,j} - 2\mathbf{x}_{i,j-1} + \frac{1}{2}\, \mathbf{x}_{i,j-2} \right) \frac{1}{\Delta\psi} \tag{25}$$

Special care must be taken in order to avoid zeros on the diagonal of the Jacobian of the discretization's functional. Therefore, tangential derivative ∂_σ is discretized on $\psi = 0, \psi = \psi_{\max}$ by the third-order differences

$$\partial_\sigma \mathbf{x}_{i,j} \approx \left(\frac{1}{6}\, \mathbf{x}_{i-2,j} - \mathbf{x}_{i-1,j} + \frac{1}{2}\, \mathbf{x}_{i,j} + \frac{1}{3}\, \mathbf{x}_{i+1,j} \right) \frac{1}{\Delta\sigma} \tag{26}$$

The overall discretization is of second order of accuracy. This accuracy of the method has been addressed by standard benchmark test cases [15] as well as by cross-validation with a different code, see Section 4.1 and Reference [12].

3.2. Solution procedure

Discretization of the inverse Euler equations yields a large system of algebraic equations

$$\mathbf{F}(\mathbf{x}^*) = \mathbf{0} \tag{27}$$

The discretized equations (27) are solved by Newton's method

$$D\mathbf{F}(\mathbf{x}^n)\Delta\mathbf{x}^n = -\mathbf{F}(\mathbf{x}^n) \tag{28a}$$

$$\mathbf{x}^{n+1} = \mathbf{x}^n + \Delta\mathbf{x}^n \tag{28b}$$

where the sequence $\mathbf{x}^n$ approximates $\mathbf{x}^*$. The linearized equations (28a) are solved by a BiCGStab iterative solver [16], preconditioned by an incomplete LU factorization. These methods are implemented in the numerical library 'Portable Extensible Toolkit for Scientific Computation' (PETSc) [17].

In addition to these standard methods, we propose a nested iterations strategy to find the initial guess for Newton's method. On a coarse grid we solve the discretized equations with Newton's method; because of the small number of unknowns a long searching phase will be cheap in terms of computing time. Once the solution on the coarse grid is known, we transfer it by bilinear interpolation to the next finer grid. The interpolated solution is used as initial guess on the finer grid. This initial guess being already very accurate, Newton's method will converge very fast, typically in 4–6 steps. We repeat this procedure until the desired accuracy is achieved. In a typical run, the nested iterations strategy reduces the computing time by a factor 6 with respect to a simple Newton method. The speedup factor increases as the final grid gets finer.

4. APPLICATION EXAMPLES

4.1. Annular diffuser

To demonstrate the capabilities of the method the inverse design of a compressor diffuser is considered. Because of the space requirements of turbine and combustor a curved diffuser is chosen. The inverse design procedure is motivated by the request of being able to avoid flow separation. In the first step the flow is computed for the baseline design (in direct mode). The resulting static pressure distribution along the side walls can be used as a starting point to define a inverse design strategy. In order to satisfy geometric constraints imposed by neighbouring parts the inner wall (the one starting at the smaller radius) remains fixed. The outer wall is a better candidate for flow separation and should be designed according to the largest admissible adverse pressure gradient, which minimizes losses and risk of separation. These considerations may lead to the following inverse boundary condition (we prescribe the specific massflow distribution):

$$m(\sigma) = \begin{cases} 1.0, & \sigma \leqslant \sigma_0 \\ 0.3, & \sigma \geqslant \sigma_0 + 5 \\ 0.65 + 0.35\cos(\pi/5(\sigma - \sigma_0)) & \text{otherwise} \end{cases} \tag{29}$$

The streamwise location σ_0 where the transition starts is left as an additional degree of freedom. In Figure 1 we present four diffusers which generate the same pressure recovery for different values of σ_0. The designer can now choose between the various shapes by applying other optimization criteria such as quality of the flow at the outlet.

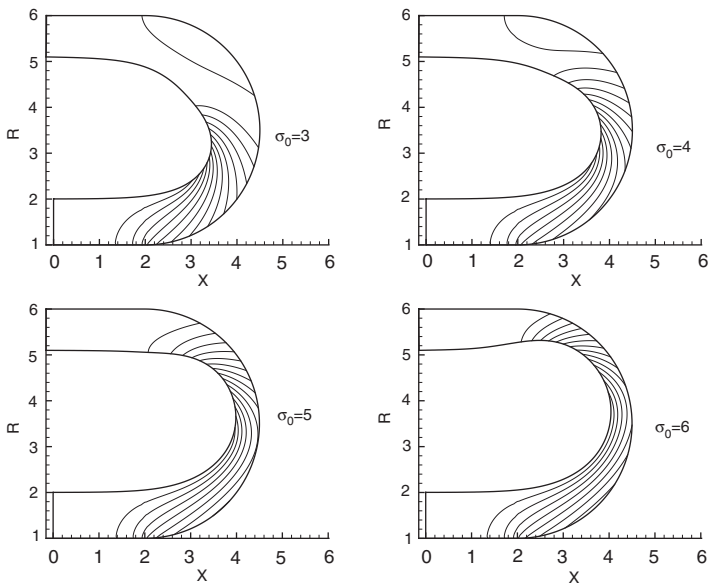

Figure 1. Inverse design of an annular diffuser: The wall starting at $r = 1$ is fixed, at the other wall a specific massflow distribution (29) is enforced. The distribution is the same for all cases up to the location of the transition between low and high pressure (parameter σ_0, which is an additional degree of freedom for the designer). The different positions of transition between the two pressure levels are clearly recognizable from the Mach number isolines. The computations have been performed on a 320×48 grid.

The results have been validated using the inviscid version of NSMB [18]. In addition, extensive grid-dependence studies have been performed. For a 320×48 grid, the solution can be assumed grid independent. The difference between in the pressure field computed by the two codes is below 0.5%, see Reference [12].

4.2. Inverse design of a turbine inlet

The second example concerns the design of a turbine inlet. We assume steady inviscid axis-symmetric flow. Although this is not an adequate model in a strong sense, it will be accurate enough for a preliminary design stage. The inner wall is kept fixed, while the outer wall is subject to inverse design. The design goal is to obtain a velocity distribution along the side walls as smooth as possible, since peaks in the velocity distribution would adversely affect heat conduction properties. The prescribed velocity distribution is shown in Figure 2(a). As mentioned above, this velocity distribution is converted to a specific massflow distribution by isentropic relations. The flow is almost incompressible as the Mach number is below 0.2. At the inlet (which is the outlet of circumferentially arranged combustor nozzles) a linear swirl profile is assumed with a relatively high circumferential velocity (50% of the meridional velocity at the inner and outer walls). The resulting geometry and the Mach number contours are shown in Figure 2(b).

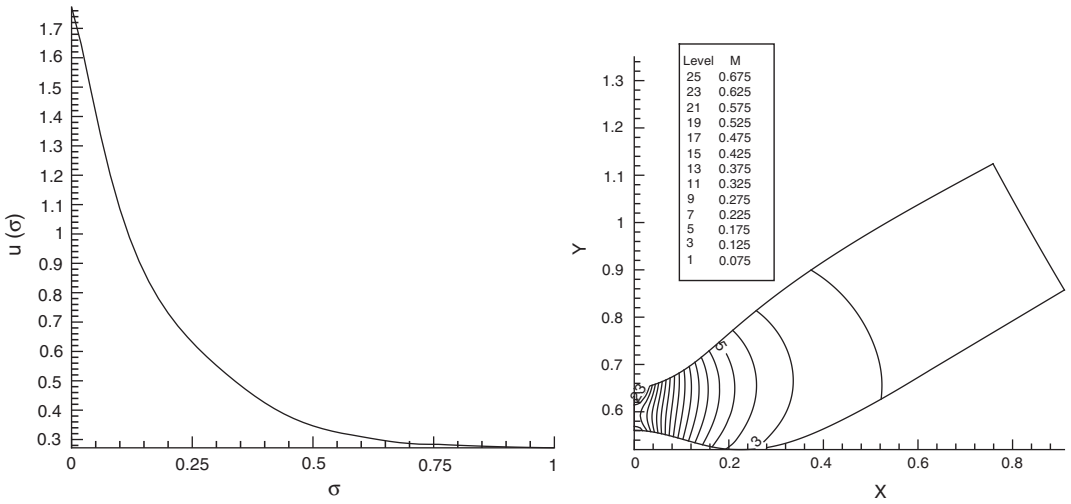

Figure 2. Inverse design of a turbine inlet: (a) prescribed velocity distribution along the upper wall. The lower wall geometry is fixed; (b) resulting geometry and Mach number field. The flow is from right to left.

5. QUASI-THREE-DIMENSIONAL FLOWS AND DISTRIBUTED LOSS MODEL

The nature of turbomachinery flows is unsteady, viscous and 3D. However, for nearly axis-symmetric configurations a 2D approach can be used if the variations in two space dimensions are more important than those in the third one. In order to treat these flow situations with limited 3D effects an intermediate description between the fully 3D and the 2D can be introduced, which is called Q3D [11].

5.1. Passage averaged equations

The basic idea is to average the flow equations over the angular co-ordinate θ and to express the averaged equations in terms of averaged quantities. For the density ρ and the pressure p we use passage averaging between pressure and suction side (subscripts p and s, respectively), while for all other quantities density weighted averaging is employed:

$$\overline{\rho} = \frac{1}{\theta_s - \theta_p} \int_{\theta_p}^{\theta_s} \rho \, \mathrm{d}\theta, \quad \rho = \overline{\rho} + \rho' \tag{30a}$$

$$\tilde{\mathbf{u}} = \frac{1}{\overline{\rho}(\theta_s - \theta_p)} \int_{\theta_p}^{\theta_s} \rho \mathbf{u} \, \mathrm{d}\theta, \quad \mathbf{u} = \tilde{\mathbf{u}} + \mathbf{u}'' \tag{30b}$$

For the sake of definiteness we repeat the passage averaged flow equations here (see e.g. Reference [11] for details; tildes and overbars are omitted for simplicity):

$$\partial_x(\rho Bru) + \partial_y(\rho Brv) = 0 \tag{31a}$$

$$u\partial_x u + v\partial_r u + \frac{1}{\rho}\,\partial_x p = F_{\mathrm{B},x} + F_{\mathrm{P},x} \tag{31b}$$

$$u\partial_x v + v\partial_r v - \frac{w^2}{r} + \frac{1}{\rho}\,\partial_r p = F_{\mathrm{B},r} + F_{\mathrm{P},r} \tag{31c}$$

$$u\partial_x C + v\partial_r C = r(F_{\mathrm{B},\theta} + F_{\mathrm{P},\theta}) \tag{31d}$$

Here the blockage factor $B = N/2\pi(\theta_s - \theta_p)$ has been introduced, where N is the number of blades. In the continuity equation no additional terms appear, since we use density averaged velocity components. The additional force terms in the momentum equations F_{B} (blade forces, flow deflection) and F_{P} (perturbation terms, deviation from average) are of the form (e.g.)

$$F_{\mathrm{B},x} = \frac{N}{2\pi B\rho}\,(p'_s\partial_x\theta_s - p'_p\partial_x\theta_p)$$

$$F_{\mathrm{P},x} = -\frac{1}{rB\rho}(\partial_x(rB\overline{\rho u''^2}) + \partial_r(rB\overline{\rho u''v''}))$$

They are determined by a blade-to-blade computation. Perturbation terms are neglected here for simplicity. The energy equation becomes (in the absence of perturbation terms)

$$u\partial_x H + v\partial_r H = \mathbf{F}\cdot\mathbf{u} + \frac{C}{r^2}\,\mathbf{u}\cdot\nabla C = \mathbf{G}\cdot\mathbf{v} = 0 \tag{31e}$$

where $\mathbf{G} = (F_{\mathrm{B},x}, F_{\mathrm{B},r}, F_{\mathrm{B},\theta})^{\mathrm{T}}$, $\mathbf{v} = (u, v, w)^{\mathrm{T}}$, $\mathbf{F}$ and $\mathbf{u}$ are the first two components of $\mathbf{G}$ and $\mathbf{v}$, respectively. For non-rotating blades the blade force is orthogonal to the local velocity vector, therefore the right-hand side of (31e) vanishes.

5.2. *Distributed loss model*

An exact prediction of loss mechanisms and loss distributions is prohibitively expensive for design purposes. However, it is possible to model the effect of shear stresses on the motion by a *distributed friction force* [10]. Empirical information (e.g. stagnation pressure drop between inlet and outlet) can be used to model entropy generation due to losses or shocks. Details of where and how losses are generated are neglected. In particular, the flow close to walls is not described correctly and it is necessary to superimpose a boundary layer approximation (see Section 6). However, the main aspects of the averaged flow can be captured correctly. The corresponding flow model is basically inviscid but not isentropic.

The basic assumptions are the following: The effect of shear stresses τ is modelled by a semi-empirical external friction force $\mathbf{G}_f$:

$$\nabla\cdot\tau \approx \rho\mathbf{G}_f = (F_{f,x}, F_{f,r}, F_{f,\theta})^{\mathrm{T}} \tag{32}$$

Here again we use the notation $\mathbf{F}_f$ and $\mathbf{u}$ for the meridional components of $\mathbf{G}_f$ and $\mathbf{v}$. Further we assume that the kinetic energy losses are compensated by heat diffusion. This is reasonable for many practical situations where the Prandtl number is close to one. In the Q3D equations (31) the external friction force $\mathbf{G}_f$ has to be added to $\mathbf{G}$.

The explicit form of $\mathbf{G}_f$ remains to be specified. At the end of this section we present an example.

5.3. Inverse equations

Since the blocking factor B appears in the continuity equation we have to change the stream function definition (3) into

$$\nabla\psi = \rho r B \mathbf{u}^{\perp}$$

Following the procedure of Section 2 the inverse Euler equations with a distributed loss model are

$$\partial_\sigma\left(\frac{J}{h^2}\partial_\sigma \mathbf{x}\right) + \partial_\psi\left(\frac{h^2}{J}\partial_\psi \mathbf{x}\right) = 0 \tag{33a}$$

$$\partial_\psi H - T\partial_\psi s - \frac{1}{\rho r B J}\,\partial_\psi\left(\frac{h^2}{\rho r B J}\right) - \frac{C}{r^2}\,\partial_\psi C = -\frac{J}{h^2}\,(\mathbf{F}+\mathbf{F}_f)\cdot\mathbf{x}_\sigma^{\perp} \tag{33b}$$

$$\partial_\sigma C = \rho r^2 B J (F_{\mathrm{B},\theta} + F_{f,\theta}) \tag{33c}$$

$$\partial_\sigma H = 0 \tag{33d}$$

$$\frac{T}{\rho r B J}\,\partial_\sigma s = \mathbf{v}\cdot\mathbf{G}_f \tag{33e}$$

The energy equation states again that the total enthalpy H is conserved along streamlines. In absence of external heat sources and shocks the external friction force is the only source of entropy generation.

5.4. Application example: quasi-three-dimensional blade channel

Here we present the application of the Q3D and distributed loss model to inverse design of a blade channel. In Figure 3(a) (tangential S_1 plane) the blade shape and the resulting blockage function B are shown. A blade-to-blade tool [19] has been used to generate the blades. The surface pressure distribution allows determination of the blade forcing terms F_{B} in the passage averaged equations. We are faced with the problem to design the shape of the casing in the meridional plane (S_2 plane, Figure 3(b)). The wall at $r=1$ is fixed, while the other one is subject to inverse design. In particular, we prescribe the meridional specific massflow

$$m = \begin{cases} 1, & \sigma \leqslant 2 \\ 0.5, & \sigma \geqslant 4 \\ 0.75 + 0.25\,\cos(\pi/2(\sigma-2)) & \text{else} \end{cases}$$

The inflow Mach number is set to 0.4. For comparison, two resulting wall shapes are shown: the lower one without and the upper one with blockage effect and blade forces.

In the next step we introduce the distributed loss model. Neglecting all local details of loss generation we assume that the external friction force is oriented anti-parallel to the meridional

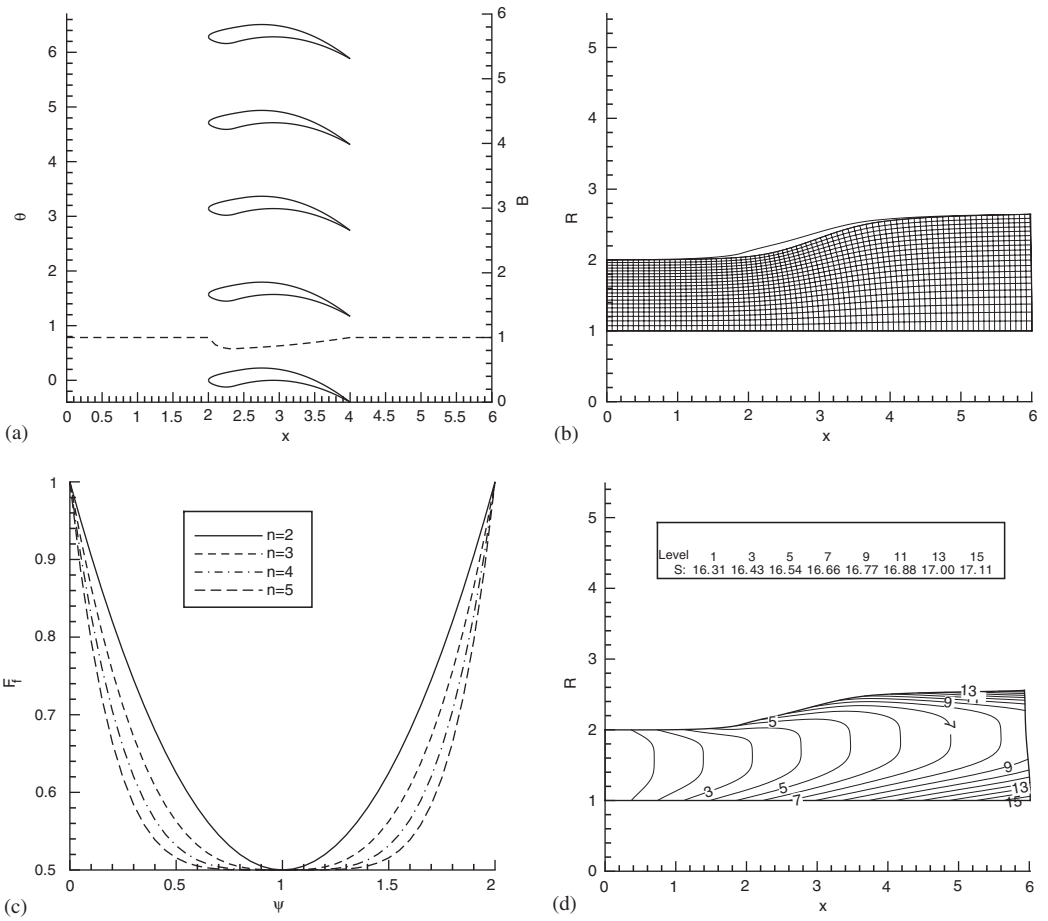

Figure 3. Q3D example: (a) tangential S_1 plane and given blade geometry (left scale), corresponding blockage factor B (dashed line, right scale); (b) meridional S_2 plane: geometry and orthogonal streamline grid with (upper contour line) and without Q3D effects; (c) profiles of friction force F_f for distributed loss model; for increasing n, losses are concentrated near the walls, in a way similar to a boundary layer; (d) resulting entropy contours for $n=2$.

velocity vector:

$$\mathbf{F}_f = -\frac{\mathbf{u}}{\|\mathbf{u}\|} F_f, \quad F_f \geqslant 0$$

The assumed spanwise friction force distribution is shown in Figure 3(c) ($n=2$): losses are concentrated near the casing. The resulting shape and the entropy contours are shown in Figure 3(d). The shape is the same as before, since the same specific massflow boundary condition is enforced as in the loss-free case. The static pressure distribution is however different because of the streamwise change of total quantities.

6. BOUNDARY-LAYER FORMULATION

It is important to take viscous effects into account at an early design stage. However, solving the full Navier–Stokes equations requires a fine grid, hence it is generally considered too expensive for design purposes. If separation regions are limited (which is indeed the aim of diffuser design), zonal approaches based on an inviscid computation and a separate boundary-layer treatment offer reasonable accuracy at dramatically reduced cost.

The idea is to solve the inverse Euler equations in the inviscid interior zone as described in Section 2.2. In the viscous near-wall zone the two-equation boundary-layer method presented in Reference [20] is employed. The main input parameters are the Mach number and velocity distribution M_e and u_e at the edge of the boundary layer. The boundary-layer method yields the displacement thickness

$$\delta^* = \int \left(1 - \frac{\rho u}{\rho_e} u_e\right) \mathrm{d}\eta \tag{34}$$

which corresponds to the thickness of a rectangular profile with same $\rho_e u_e$ and total massflow [21]. The physical boundary of the interior inviscid computation therefore must be displaced by δ^*. For an inverse wall the edge velocity u_e can be determined *a priori* from the prescribed pressure distribution by the isentropic relations [4]. δ^* is then simply added to the resulting inviscid geometry. For a direct computation u_e is not known in advance; it results in turn from the solution in the inviscid interior (for a given displacement thickness).

If this coupling is treated explicitly the convergence behaviour may be poor. Therefore, we choose to solve the boundary-layer equations along with the inviscid flow equations. Moreover, the boundary-layer ODEs are stiff and must be discretized with an implicit scheme. For unseparated boundary layers the trapezoidal rule has shown to produce sufficiently accurate results. Implicit discretization of the boundary layer equations and implicit coupling of boundary-layer treatment and flow computation fit well into the framework of a full Newton solver described in Section 3.2.

We apply this formulation to the inverse design of a 3D diffuser. The Reynolds number is $Re = 9.7 \times 10^5$, the inflow Mach number $M = 0.2$, and the inlet boundary-layer thickness is approximately 10% of the channel height. The lower wall is kept fixed at $y = 0$, while the upper one is subject to inverse design. We impose the specific massflow distribution in such a way that the adverse pressure gradient remains below a critical value (we try to avoid separation):

$$m(\sigma) = \begin{cases} 1 & \sigma \leqslant 2 \\ \dfrac{1}{2}\left(1 + \dfrac{1}{1 + (x-2)^2/10}\right) & \text{else} \end{cases}$$

Figure 4 shows the computational domain in the inviscid region. The growth of the displacement thickness is well visible in the regions of adverse pressure gradient. The corresponding inviscid solution is shown in the lower figure.

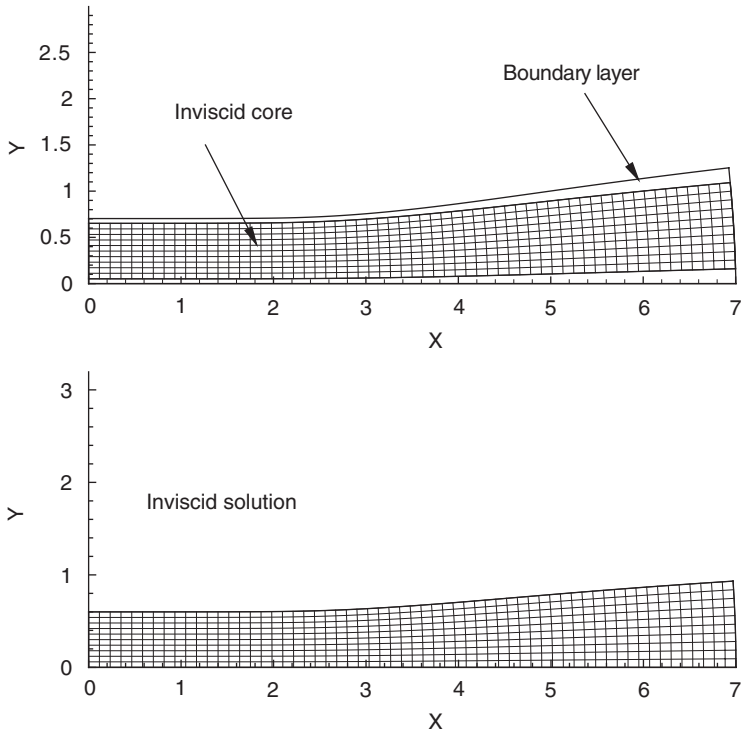

Figure 4. 2D diffuser. Comparison of an inviscid design with a design taking into account a laminar boundary layer.

7. CONCLUSION

We presented a hierarchy of flow models and their inverse formulation in the framework of the inverse Euler equations of Keller [4, 5]. Starting from the basic rotational axis–symmetric flow equations we added features for handling losses by a frictional force which can be calibrated to match experimental data and for handling blockage and forces due to the presence of blades. These novel formulations of the inverse Euler equations replace the 3D inverse equations, which have been shown to hold only for a limited class of flows, and in particular not to be valid for general 3D duct flows. In a series of numerical examples we showed the influence of the new terms in the inverse Euler equations. Current research toward a 3D design tool consists in defining a system of co-ordinates which is flow aligned only along the side walls, and solving the resulting grid generation and flow equations in a coupled way.

ACKNOWLEDGEMENTS

The first two authors would like to thank Dr T. Sommer for many helpful discussions.

REFERENCES

1. Jameson A, Martinelli L, Pierce NA. Optimum aerodynamic design using the Navier–Stokes equations. *Theoretical Computer Fluid Dynamics* 1998; **10**:213–237.
2. Demeulenaere A, van den Braembussche R. Three-dimensional inverse method for turbomachinery blading design. *ASME Journal of Turbomachinery* 1998; **120**(2):247–255.
3. Troxler A, Scascighini A. Inverse design for 2D internal flows. In *Proceedings of the 5th ISAIF Conference*, Gdansk, September 2001.
4. Keller JJ. Inverse Euler equations. *Zeitschrift für Angewandte Mathematik und Physik* 1998; **49**:363–383.
5. Keller JJ. Inverse equations. *Physics of Fluids* 1999; **11**:513–520.
6. Zannetti L. A natural formulation for the solution of two-dimensional or axis-symmetric inverse problems. *International Journal for Numerical Methods in Engineering* 1986; **22**:451–463.
7. Dedoussis V, Chaviaropoulos P, Papailliou K. Rotational compressible design method for two-dimensional internal flows. *AIAA Journal* 1993; **31**:551–558.
8. Stanitz JD. A review of certain inverse methods for the design of ducts with 2- or 3-dimensional potential flows. In *Proceedings of the Second International Conference on Inverse Design Concepts and Optimization in Engineering Sciences*, Penn State University: University Prak, PA, 1987.
9. Chaviaropoulos P, Dedoussis V, Papailliou KD. On the 3D inverse potential target pressure problem. Part 1: theoretical aspects and method formulation. *Journal of Fluid Mechanics* 1995; **282**:121–146.
10. Hirsch C. *Numerical Computation of Internal and External Flows*, vol. 1. Wiley: Chichester, 1988.
11. Hirsch C, Deconinck H. Through flow models for turbomachines: stream surface and passage averaged representations. In *Thermodynamics and Fluid Mechanics of Turbomachinery*, Ucer S, Stow P, Hirsch C (eds.). vol. 1, NATO ASI Series. Martinus Nijhoff: Dordrecht, 1985.
12. Scascighini A. A numerical method for the design of internal flow configurations based on the inverse Euler equations. *Diss. ETH No.* 14440, 2002.
13. Knupp P, Steinberg S. *Fundamentals of Grid Generation*. CRC Press: Boca Raton, 1994.
14. Panton R. *Incompressible Flows*. Wiley: Chichester, 1984.
15. Périaux J *et al. EUROPT A European Initiative on Optimum Design Methods in Aerodynamics*, vol. 55, Notes on Numerical Fluid Mechanics. Vieweg: Braunschwig, 1997.
16. van der Vorst HA. Bi-CGSTAB: a fast and smoothly converging variant of Bi-CG for the solution of non-symmetric linear systems. *SIAM Journal on Scientific and Statistical Computing* 1992; **13**:631–644.
17. Balay S, Gropp WD, McInnes LC, Smith BF. PETSc users manual. *Technical Report ANL*-95/11—*Revision* 2.1.0, Argonne National Laboratory, 2001.
18. Vos VB *et al. NSMB Handbook Version* 4.5, 2001.
19. Drela M. XFOIL: an analysis and design system for low Reynolds number airfoils. In *Low Reynolds Number Aerodynamics*. Mueller TJ (ed.). Springer: Berlin, 1989.
20. Drela M, Giles MB. Viscous-inviscid analysis of transonic and low Reynolds number airfoils. *AIAA Journal* 1987; **26**(10):1347–1355.
21. Cebeci T, Smith AO. *Analysis of Turbulent Boundary Layers*. Academic Press: New York, 1974.

